Prediction of diagenetic facies using well logs – A case study from the Upper Triassic Yanchang Formation, Ordos Basin, China

Yufeng Cui[a, b], Guiwen Wang[a], Stuart J. Jones[b], Zhenglong Zhou[a], Ye Ran[a], Jin Lai[a], Ruijie Li[a], Li Deng[a]

[a] State Key Laboratory of Petroleum Resources and Prospecting, China University of Petroleum, Beijing 102249, China

[b] Department of Earth Sciences, Durham University, South Road, Durham, DH1 3LE, UK

Abstract

Understanding diagenetic heterogeneity in tight sandstone reservoirs is important for hydrocarbon exploration. The seventh unit of the Upper Triassic Yanchang Formation in the Ordos Basin (Chang 7 unit), central China, is an important oil-producing interval. Results of helium porosity and permeability and petrographic assessment from thin sections, X-ray diffraction, scanning electron microscopy and cathodoluminescence analysis demonstrate that the sandstones have encountered various diagenetic processes encompassing mechanical and chemical compaction, cementation by carbonate, quartz, clay minerals (illite, I/S mixed layer, chlorite and kaolinite), and dissolution of feldspar and lithic fragments. The sandstones comprise silt- to medium-grained lithic arkoses to feldspathic litharenites and litharenites, which have low porosity (0.5% to 13.6%, with an average of 6.8%) and low permeability (0.009×10^{-3} μm^2 to 1.818×10^{-3} μm^2, with an average of 0.106×10^{-3} μm^2).

This study suggests that diagenetic facies identified from petrographic observations can be up-scaled by correlation with wireline log responses, which can facilitate prediction of reservoir quality at a field-scale. Four diagenetic facies are determined based on petrographic features including intensity of compaction, cement types and amounts, and degree of dissolution. Unstable and labile components of sandstones can be identified by low bulk density and low gamma ray log values, and those sandstones show the highest reservoir quality. Tightly compacted rocks, which tend to have high gamma ray readings and relatively high bulk density values, show the poorest reservoir quality. A model based on principal component analysis (PCA) is

built and show better prediction of diagenetic facies than biplots of well logs. The model is validated by blind testing log-predicted diagenetic facies against petrographic features from core samples from Upper Triassic Yanchang Formation of the Ordos Basin, which indicates it is a helpful predictive model.

Key word: diagenetic facies, rock typing, well logs, tight sandstone reservoir, principal component analysis

Introduction

Porosity and permeability of sandstone reservoirs play an important role in hydrocarbon exploration, controlled by numerous factors such as sand composition and grain size, texture, pore-fluid chemistry, temperature and effective stress. These variables and others have been the focus of many recent studies (e.g. Nguyen et al., 2013; Salem et al., 2000; Stricker et al., 2016a; Taylor et al., 2010; Yuan et al., 2015). Variations in the above controlling factors result in reservoir heterogeneity at various extends and scales, ranging from micrometers to hundreds of meters (Morad et al., 2010). Thus, reservoir evaluation is achieved by dividing reservoirs into relatively homogeneous subgroups based on a set of criteria obtained from core analysis and petrophysical analysis, and subsequently evaluated in each subgroup. To that end, hydraulic units, lithofacies, petrofacies and electrofacies have been mentioned in several studies (Amaefule et al., 1993; Perez et al., 2005; Porras et al., 1999). Similarly, Rushing et al. (2008) proposed three rock types (i.e. depositional, petrographic and hydraulic) to estimate rock properties of tight gas sandstones. Meanwhile, diagenetic rock types, i.e. diagenetic facies, are used by Grigsby and Langford (1996) and Ozkan et al. (2011) to describe diagenetic heterogeneity in reservoirs. Diagenetic facies refer to interval or unit features formed by diagenetic processes interacting with sediments under certain tectonic settings. In other words, diagenetic facies is a terminology used to classify and/or distinguish intervals or units by taking compaction, cement types and textures, dissolution and so on into consideration (Liu et al., 2015; Zou et al., 2008).

As the costs of coring are high and only limited intervals are cored, it is critical to upscale diagenetic features by correlation with well logs for subsequent field scale reservoirs quality evaluation. However, prediction of diagenetic features using well logs is relatively poorly explored in literatures. One of the few examples is that of Serra (1986) who listed the log characteristics of diagenetic minerals in sedimentary rocks, and provided plentiful evidence to indicate the viability for prediction of diagenetic alterations using well logs. Another example is that of Ozkan et al. (2011) and they translated petrographic features to log responses (i.e. gamma ray, bulk density and deep resistivity) to generate a model which can be used to predict diagenetic facies.

This study aims to partition the rocks into several relatively homogeneous diagenetic facies, and correlate them with well logs to build a model to predict diagenetic facies in uncored intervals. Multiple methods including thin section analysis, X-ray diffraction, scanning electron microscope, cathodoluminescence have been performed to illustrate the diagenetic features based on the core samples from Chang 7 unit in Upper Triassic Yanchang Formation, Heshui Field, Ordos Basin, north central China. Moreover, helium porosity and permeability have been examined to obtain reservoir quality. Techniques of biplots and principal component analysis (PCA) also have been used to build the model for prediction of diagenetic facies. In addition, a log suit containing gamma-ray, spontaneous potential, bulk density, thermal neutron porosity, borehole-compensated sonic, array induction and dual induction laterlog has been collected to correlate with diagenetic facies.

1. Geological setting

The Ordos Basin is one of the oldest and most important non-marine hydrocarbon provinces in China (Qiu et al., 2014). The basin is located in the central part of north China block (Fig. 1) with an area of 320 000 km^2 (Liu et al., 2004; Yang et al., 2010). It accounts for approximately one third of the total oil and gas output of China and has huge resource potential and abundant oil resources are present in the Upper Triassic Yanchang Formation (Yang and Deng, 2013; Zeng and Li, 2009; Zhong et al., 2013; Zhu et al., 2008).

During the Early to Middle Triassic, the Ordos Basin was part of the North China intracratonic depression, with sedimentary systems dominated by a fluvial-lacustrine depositional setting. As a consequence of regional collisional tectonism and related intra-plate deformation in the Late Triassic (Vermeesch, 2012), the Ordos Basin evolved into a foreland basin, characterized in its asymmetric cross-section by low-gradient north-eastern and high-gradient south-western flanks, and dominated by fluvial and lacustrine depositional systems during much of the Late Triassic (Figs 1 & 2; Henares et al., 2014; Wang et al., 2016). Six tectonic units in the Ordos Basin have been identified, i.e., the Yimeng Uplift in the north, the Western Trust Belt on the west margin, the Tianhuan Depression in the west, the Yishan Slope in the center, the Weibei Uplift in the south, and the Jinxi Fault-Fold Belt in the east (Fig. 1). These tectonic units produced orogenic highlands and acted as sediment sources around the basin margin. Of these, Yimeng Uplift and Western Thrust belt

were the most important source areas as determined from predominantly north-eastern and south-western progradational directions of fluvial-deltaic systems in the Ordos Basin. The Yishan slope, which covers the largest area of the Ordos Basin, dips at less than 1° toward the west. The study area is located in the southwestern region of Yinshan Slope (Fig.1).

The Early and Middle Triassic climate of the Ordos Basin was semi-arid to arid, and the fluvial strata in northern Ordos Basin were dominated by redbeds with calcic palaeosols. However, the paleoclimate gradually became humid in the Late Triassic. Interbedded dark shale and coal seams developed, except at the base of the Yanchang Formation (Fig.2).

2. Yanchang Formation Stratigraphy

The Late Triassic Yanchang Formation is dominated by fluvial, lacustrine and deltaic sedimentation with a thickness of between 1000 - 1300 m throughout most of the Ordos Basin (Fig.2; Qiu et al., 2015; Zou et al., 2012). The sequence of the Yanchang Formation is subdivided into 10 informal oil reservoir units named Chang 1 to Chang 10 from top to bottom, based on marker beds, sedimentary cycles and lithological associations (Fig 2; Guo et al., 2014; Ji et al., 2008; Qiu et al., 2015). Oil reservoir units Chang 10 to Chang 8 were deposited during the expanding stage in the Middle Triassic of the lake basin, which later reached its highstand (i.e. maximum expanding period) during the deposition of Chang 7 unit. Reservoir units Chang 6 to Chang 4 mark a gradual shallowing of the lake basin and a predominantly fluvial facies association. Units of Chang 3 to Chang 1 are recognized as the continued fluvial

sedimentation.

Oil shale, black shale and carbonaceous shale in bottom of Chang 7 constitute the best source rocks of Yanchang formation (Duan, 2012; Duan et al., 2008; Zhang et al., 2009). The source rocks are mainly humic-sapropel type and minor sapropel type and the R_o values of the source rocks range from 0.66% to 1.07% (Duan et al., 2008; Zhao et al., 1996). In the last decades the source rocks from Chang 7 unit, which could be used for oil-source rock correlation and thus facilitate hydrocarbon exploration, have attracted much attention (e.g. Ma et al., 2005; Xi et al., 2008; Zhang et al., 2009). However, in recent years, debris flows and turbidity sandstones at the top of Chang 7 have been found as oil and gas reservoirs, which are known as tight sandstone reservoirs (Yang et al., 2010).

3. Methodology

Well logs

Wireline logs used in the study area include gamma-ray (GR), spontaneous potential (SP), bulk density (DEN), thermal neutron porosity (CNL), borehole-compensated sonic (AC), array induction (AT10, AT20, AT30, AT60 and AT90), and dual induction laterolog (RILD, RILM and RLL8). In this study, we regard AT90 (or RILD in some wells) as the deep resistivity (RT).

Petrography

Core and cutting samples were collected from 35 wells, representing Chang 7 unit

including upper delta facies and lower lacustrine facies (Fig. 2), and the core-to-log depth matching was done by correlating the DEN signature with the core experiment analysis. Routine core analyses, including helium porosity and permeability, and density of 1060 core samples with 1 in diameter (2.54 cm) from the wells were examined. 203 representative core samples were impregnated with red epoxy resin under vacuum (this is different with traditionally blue resin, but calcite, stained with Alizarin Red S and potassium ferricyanide, can be discriminated with cleavages from pores under plane-polarized light) and thin sectioned. Point counting of at least 300 points per slide was performed on these thin sections to determine the modal composition of grains, cement content, porosity, and intergranular volume. These thin sections were also stained with Alizarin Red S and potassium ferricyanide to identify carbonate cements (i.e. calcite, ferroan calcite, dolomite and ankerite). The sorting values are determined from 137 transparent thin sections by measuring the long axes of at least 300 grains per thin section. Cathodoluminescence (CL) analysis of 55 polished thin sections were measured by a Technosyn cold cathode luminoscope, with the acceleration voltage of 20 kV, 200-400 mA, to identify cementation, grains and timing of cementation (Boggs and Krinsley, 2006). X-ray diffraction (XRD) analysis of 43 samples on clay fractions and bulk fractions was performed for identification of the clay mineral types and amounts. 180 representative sandstone samples were coated with gold and examined with a JEOL JSM-T330 scanning electron microscope (SEM) to analyze clay mineral types, petrography texture and pore space morphology.

Techniques to build and validate the model

Diagenetic facies are identified on the basis of petrographic characteristics, obtained from above methods, including diagenetic minerals, pore types, intensity of cementation and compaction. A calculation procedure based on PCA algorithm from Jolliffe (2002) was generated through the Matlab software, then principal components of selected well log values are calculated. By correlating the diagenetic facies with well logs and principal components, crossplots based on well logs and principal components grouped by diagenetic facies are compared and the best one is selected as the model to distinguish diagenetic facies. Validation of the model is performed by application in Cheng 96 well, in which the predicted diagenetic facies are compared with petrographic features at corresponding depth, using the software of Formation Oil & Gas Reservoir Well Logging Analysis & Research & Development (FORWARD copyright by CNPC Exploration Department).

4. Results

4.1 Grain texture and composition, and sedimentary structure

The sandstones from Chang 7 unit are mostly very fine-grained (average 111 μm) with a wide grain size range from 40 μm to 420 μm, and moderately sorted with an average sorting value 0.9 (from 0.6 to 1.9 expressed as sigma phi). Grain roundness ranges from subangular to subrounded. Monocrystalline quartz with uniform to slightly undulose extinction ranges from 12% to 65% with an average of 39% among framework grains. Feldspar content varies from 9% to 46% (average 22%; among

framework grains), consisting of plagioclase and potassium feldspar (mostly microcline and perthite). Rock fragments range from 20% to 61% with an average of 39% among framework grains. The component of rock fragments consists mainly of average 65% metamorphic rock fragments, and average 25% igneous rock fragments, and trace amount of chert, argillaceous sedimentary fragments. Matrix is mostly depositional matrix including mainly clays, hydromica and tuff, and minor amount of clay-size quartz and feldspars. The cements are mainly carbonate and clay minerals, along with trace to minor amount of quartz cements, pyrite and zeolite. According to Folk's classification (Folk, 1974), Chang 7 unit are identified as lithic arkoses, feldspathic litharenites and litharenites (Fig. 3).

Parallel bedding and massive bedding are encountered in Chang 7 unit as indicated from core samples (Fig. 5A, D). Sub-rounded mud peddles show directional features in these sandstones (Fig. 5B). Contemporaneous deformation structures (mainly flame structure and convolute bedding) appear commonly in Chang 7 unit (Fig. 5C, F). Lithic fragments containing black carbonized plants and/or horizontal bedding also occurs in core samples (Fig. 5E).

4.2 Porosity, Permeability and Pore Types

Based on the conventional core experiment of 1060 samples, porosity ranges from 0.5% to 13.6%, with an average of 6.8%, and horizontal permeability ranges from 0.009×10^{-3} μm^2 to 1.818×10^{-3} μm^2, averaged 0.106×10^{-3} μm^2 (Fig. 5). The correlation between porosity and permeability is weak (R^2=0.39). Few samples are characterized

by high porosity with low permeability, or low porosity with high permeability (Fig. 5). Thin section porosity including primary intergranular porosity and secondary porosity (Fig. 6A, B) vary from trace to 10.0% with an average of 2.1%. Primary intergranular porosity (Fig. 6A, B) varies from trace to 8% with an average of 1 %. Secondary porosity, ranging from trace to 4%, averaged at 1%, results mainly from dissolution of feldspars (Fig. 6A, B) and rock fragments. Abundant clay minerals occlude pores or coat grains (Fig. 6A-C). Pores cemented with carbonates in these thin sections show little intergranular pore space (Fig. 6B). Limited amount of micro-fractures also can be observed by scanning electron microscopy (Fig. 6D). Though micropores (<5 μm) are difficult to be quantified by petrographic microscope in this study (Fig. 6), various amounts of micropores have been documented (Niu et al., 2013; Xinquan et al., 2013) in Chang 7 sandstone.

4.3 Diagenetic minerals

Diagenetic minerals in Chang 7 unit contain mainly clays (av. 6.9% among bulk samples), quartz (av. 0.79% among bulk samples), ferroan calcite (av. 2.44% among bulk samples), ankerite (av. 1.45% among bulk samples) and calcite (av. 0.32% among bulk samples), and trace amount of pyrite, siderite, dolomite and feldspar overgrowth.

Quartz cements

Quartz cements, in forms of mainly syntaxial overgrowths (Fig. 7A) and minor amount of euhedral quartz crystals (Fig. 7B), can be observed through microscope and

SEM, but mostly occur in limited amount varying from trace to 4%, with an average of 0.8%. The boundary between the overgrowths, with thickness ranging generally from 3 μm to 40 μm, and grains is either poorly outlined or delineated by fluid inclusions and/or thin clay coatings. The euhedral quartz crystals (mainly less than 35 μm) fill intergranular space adjacent to quartz overgrowths, or present in secondary intragranular pores of dissolved feldspars (Fig. 7B). Rare microquartz coatings occur in the study area.

Carbonate cements

Carbonate cements are much localized throughout the Chang 7 sandstones, and encompass mainly ferroan calcite (57% among carbonate cements), ankerite (34% among carbonate cements) and calcite (7% among carbonate cements), and show various existence textures, such as scattered patches and pervasive cement (Fig. 6B; Fig. 7C-E). .

Non-ferroan calcite and ferroan calcites present as intergranular pore-filling cements, displaying poikilotopic tecture (Fig. 7C) or euhedral massive texture (Fig. 7E). Scattered euhedral crystals of ankerite occur mainly as pore-filling cements and sometimes as framework-grain replacive rhombs (Fig. 7F). Previous article (Shi et al., 2003) documented that the $\delta^{13}C$ values of calcite, ferroan calcite and ankerite range from -0.31‰ to -3.3‰, from -3.23‰ to -8.02‰ and from 0.84‰ to -1.92‰ respectively, whereas the $\delta^{18}O$ values range from -19.5‰ to -22.1‰, from -19.7‰ to -22.9‰ and from 12.6‰ to 20.5‰, respectively.

Clay minerals

Various types of clay minerals including chlorite, illite, I/S mixed layers and kaolinite, with various textures, constitute averagely 6.9% of bulk samples (Fig. 7G-I). Generally, diagenetic clay minerals occur as pore fills and bridges (Fig. 7G), along with minor grain coatings (Fig. 7H) and replacement (Fig. 7I).

Illite, the most common diagenetic clay, ranges from trace to 10.7% with an average of 3.5% among bulk samples and constitutes averagely 51% of diagenetic clay minerals. I/S mixed layers present with less amount, varying from trace to 4.9% with an average of 1.6%. The SEM examinations reveal that illite and I/S mixed layers occur in the form of pore fills and pore bridges (Fig. 7G). Limited amount of chlorite (trace to 2.9%, av. 1.4%) exists as grain coats and pore fills (Fig. 7H) and minor amount of kaolinite (av. 0.4%) occur as grain replacement (Fig. 7I).

4.4 Compaction

Evidences of mechanical compaction in Chang 7 unit are formation of ductile grains such as bending of mica plates, and concavo-convex contacts (Fig. 7J). Minor chemical compaction is evidenced by and sutured grain contacts.

Intergranular volume (IGV), or minus-cement porosity (P_{mc}), is reported as the sum of depositional matrix, intergranular pore space and the volume of cement that fills primary porosity (Paxton et al., 2002; Salomons et al., 1978). Rossi and Alaminos (2014) used 45% as initial IGV of sandstones with sorting value 1.0 phi, which is very

close to the average sorting value of this study (0.9 phi), and the stabilized IGV can be approximately calculated by subtracting 10 percent units from initial IGV (i.e. about 40%). Therefore, it seems reasonable to assume the maximum initial stabilized porosity is about 40% in this study.

It is clear from the plot of COPL versus CEPL (Fig. 8; Lundegard, 1992) that COPL values range from 9.3% to 36.7% with an average of 28.6%. And CEPL values vary from 2.7% to 30.7% with an average of 10.7%.

4.5 Secondary pores

Secondary intragranular to moldic pores (up to 4% of bulk sandstones) formed by the dissolution of feldspars and rock fragments are clearly observed (Fig. 7F, K, L). Porosity after dissolved feldspars and rock fragment constitute 82% and 10% of total secondary porosity, respectively. Some dissolved pores are partly filled with diagenetic minerals such as quartz (Fig. 7B) and carbonate (Fig. 7F). Dissolution of quartz grains and carbonate cements is rare.

4.6 Diagenetic facies

Four diagenetic facies are identified based on features of primary depositional and diagenetic features mainly focusing on porosity modification by cementation, compaction and dissolution. Petrographic as well as porosity and permeability characteristics of the four diagenetic facies are listed in Table 1, and four representative photographs for each diagenetic facies are provided in Figure 9. The

four sandstone diagenetic facies include sandstones with dissolved unstable components (Fig. 9A), sandstones with clay minerals cements (Fig. 9B), sanstones with carbonate cementes (Fig. 9C) and tightly compacted sandstones/siltstones (Fig. 9D).

4.7 Diagenetic facies identification using well logs

The available well logs in the study area contain gamma-ray (GR), spontaneous potential (SP), bulk density (DEN), thermal neutron porosity (CNL), borehole-compensated sonic (AC), array induction (AT10, AT20, AT30, AT60 and AT90) and dual induction laterolog (RILD, RILM and LL8). By correlating core samples with log values in matched depth, a database including 88 core samples was created with the log responses ranges for each diagenetic facies (Table 2).

Crossplots

GR is plotted against DEN, AC, CNL and deep resistivity (RT; AT90 in array induction logs and RILD in dual induction laterlog) to identify four diagenetic facies (Fig. 10). Considering limited range of SP values (1.2 mV to 6.7 mV) in different facies (Table 2), SP is not applied for identification of diagenetic facies. Sandstones with dissolved unstable components tend to have low GR values (71 API to 109 API; av. 88 API) (Fig. 10A; Table 2). These sandstones have low density values (<2.542 g/cm^3) (Fig. 10A; Table 2), medium to high AC values (222 μs/m to 280 μs/m; av. 240 μs/m) and relatively high neutron porosity (13% to 36%; av. 22%) (Fig. 10B, C; Table

2). However, resistivity values range widely from 10 Ω·m to 70 Ω·m (Fig. 10D; Table 2).

The clay cemented sandstones have medium GR values (68 API to 101 API; av. 87 API) (Fig. 10A; Table 2), low to medium density (2.499 g/cm^3 to 2.584 g/cm^3, av. 2.543 g/cm^3), medium to high neutron porosity values (11% to 18%, av. 14%), medium AC values (205 μs/m to 233 μs/m; av. 225 μs/m) (Fig. 10A-C; Table 2), and medium to high resistivity values(31 Ω·m to 90 Ω·m; av. 68 Ω·m) (Fig. 10D, Table 2).

Carbonate cemented sandstones have high density values (>2.548 g/cm^3), low GR values (<96 API) (Fig. 10A; Table 2), low AC values (203 μs/m to 229 μs/m), low to medium CNL values (11% to 18%) (Fig. 10B, C; Table 2), and medium to high resistivity values (18 Ω·m -98 Ω·m, av. 52 Ω·m) (Fig. 10D; Table 2).

Tightly compacted sandstones/siltstones tend to have relatively high density log readings (2.49 g/cm^3 to 2.696 g/cm^3, av. 2.548 g/cm^3) (Fig. 10A; Table 2) due to little pore space in tight compaction layers (Fig. 7J, 8D). Compared with carbonate cemented sandstones, the similar density values occur in tightly compacted sandstones/siltstones, whereas tightly compacted facies are featured with a wide range of GR values from 96 API to 155 API (Fig. 10A; Table 2) and relatively high neutron porosity varied from 11% to 47%, averaged at 17% (Fig. 10C; Table 2). In addition, tightly compacted sandstones/siltstones have a wide range of resistivity values from 8 Ω·m to 98 Ω·m (av. 40 Ω·m) and medium AC values from 203 μs/m to 258 μs/m with an average of 225 μs/m (Fig. 10B, D; Table 2).

Principal component analysis

Principal component analysis (PCA) was performed in Matlab on DEN, AC, DEN, CNL, RT and three principal components were extracted, together explaining about 85% (P1: 44%; P2: 25%; P3: 16%) of the information involved in the initial variables. P1 is plotted against P2 and P3 (Fig. 11) to discriminate diagenetic facies. Sandstones with dissolved unstable components are easily to be identified with higher P2 values (P2>0.4) than other sandstones (Fig. 11A). Tightly compacted sandstones/siltstones are featured with low P1 values (P1<0.6) and low P2 values (P2<0.4) (Fig. 11A). Both sandstones with clay minerals cements and carbonate cements are characterized by high P1 values (P1>0.6), whereas intermediate P2 values (-0.5<P2<0.4) occur in sandstones with clay minerals cements and low P2 values (P2<-0.5) exist in sandstones with carbonate cements (Fig. 11A). However, all diagenetic facies have a wide range of P3 values and could not be discriminated with P3 values (Fig. 11B).

5. Discussion

Effects of diagenetic alterations on reservoir quality

Though it is difficult to acquire precise timing and duration of diagenesis, a rough paragenetic sequence of diagenetic processes was built (Fig. 12) on the basis of petrographic examination, and previous studies (Lai et al., 2016; Mansurbeg et al., 2012; Ren et al., 2014; Shi et al., 2003). These diagenetic alterations have various effects on reservoir properties, i.e. porosity and permeability.

Similar with other works (Gluyas and Cade, 1997; Paxton et al., 2002; Stricker et al., 2016b), compaction is the predominant mechanism of porosity loss in this study, whereas cementation exerts much less important effects on reservoir quality.

Plots of secondary porosity versus porosity and permeability indicate that dissolution of unstable components (mainly feldspars) plays a significant role in enhancing porosity and permeability (Fig. 13). Secondary porosity could constitute up to 30% of total porosity (Fig. 13A). Permeability is about 0.2×10^{-3} μm^2 higher in core samples with high secondary porosity (>3%) than in the samples with low secondary porosity (<1%) (Fig. 13B). The positive relationships suggest that the dissolution of unstable components may form in open sandstone systems (Yuan et al., 2015).

Porosity and permeability have negative relationships with total content of clay minerals (Fig 13). Fibrous and flake-like illitic clays occlude intergranular pores (Fig. 6C; Fig. 7G), which resulted in increase of microporosity and decrease of total porosity and permeability (Xi et al., 2015; Yuan et al., 2015). Although part of the chlorite occurs as grain coats inhibiting compaction and quartz overgrowths, and thus preserve porosity (Ozkan et al., 2011; Stricker et al., 2016a; Taylor et al., 2010), the porosity and permeability decrease with chlorite content increasing (Fig. 13), which is probably because the grain coats are relatively thick (about 6 μm) compared with pore size (averaged approximately 25 μm) and chlorite also occur as pore filling cements (Fig. 7H). Porosity and permeability show negative relationship with carbonate cements content (Fig. 13) (see also Bowman, 1998; Xi et al., 2015). Conversely, there is no significant relationship between quartz cement content and reservoir properties

(Fig. 13) due to the small amount of quartz cement.

Significance of diagenetic facies for reservoir quality evaluation

Relationships of porosity and permeability grouped by diagenetic facies in Chang 7 unit (Fig. 14) indicate that sandstones with dissolved unstable components have the highest reservoir quality (Fig. 13). The poorest reservoir quality occurs in tightly compacted sandstones/siltstones. In the plot of porosity versus permeability (Fig. 14), the long axes slope of four ellipses show significant difference with various diagenetic facies ($k_{F3} < k_{F1} < k_{F2} < k_{F4}$). There is no clear correlation between porosity and permeability in tightly compacted facies, i.e. there is a wide range porosity values for each permeability value, and vice versa (Fig. 14), which probably results from varied pore tortuosity, scattered micro-fractures (Fig. 6D), and measuring error. With porosity increasing, permeability increases more in clay minerals cemented diagenetic facies than in secondary porosity facies and carbonate cemented facies (Fig. 14), indicating that permeability are more sensitive to porosity in sandstones with clay minerals cements than in other sandstones, which may because pores from decreasing of clay minerals are more connective in sandstones with clay minerals cements. Thus further prediction of reservoir quality could be improved by construction models within subgroups (Ozkan et al., 2011).

Mechanism of prediction diagenetic facies using well logs

Wireline logging is performed in the subsurface with present formation

condition, and hence interpretation from well logs could give a picture of the final state of the rock resulted from depositional environment and a series of diagenetic processes (Serra, 1986). The ultimate results are various in different diagenetic facies, which benefits discrimination of them.

In general, clay minerals and matrix account for appreciable amount of gamma rays (Serra, 1984). Thus tightly compacted sandstones/siltstones with abundant matrix and silts have higher GR values, whereas sandstones with dissolved unstable components tend to have lower GR readings due to low clay minerals and matrix. Sandstones with pervasive carbonate cements also show low GR values due to low gamma radioactivity of carbonate. DEN, CNL and AC could be used to evaluate compaction as they are sensitive to porosity, which would decrease with the intensity increase of compaction (Serra, 1986), along with values increase of DEN, CNL, AC apart from other factors. In addition to the porosity, composition of the sandstones also controls the DEN values. Hence, relatively low DEN readings occur in sandstones that are porous owing to the dissolution of framework grains, while higher DEN values present in other facies (relatively low porosity), especially in sandstones with carbonate cements due to high carbonate density. The quantity of clay minerals (shale volume) has significant effect on CNL, because clay minerals are likely to contain bound hydrogen (Chen and Liu, 1994), and hence tightly compacted sandstones/siltstones with high matrix have high CNL readings. However, a little lower CNL values occur in sandstones with clay minerals cements than in sandstones with dissolved unstable components, because sandstones with clay minerals cements

have lower porosity but higher clay minerals than sandstones with dissolved unstable components, and pore fluid contributes more to CNL than clay minerals (Serra, 1986). Previous studies indicate that sonic log can also be used to predict clay and carbonate cement contents (Cosenza et al., 2014; Selley, 1992). Though resistivity is mentioned to respond more to fluids than matrix (Ozkan et al., 2011), it can be used to study the degree of compaction (Serra, 1986). Resistivity can also be used to identify sandstones with carbonate cements with relatively high RT values, and tightly compacted sandstones/siltstones with relatively low RT readings. This distinction is possible because of the high resistivity of carbonates and the low resistivity of clay matrix in the two facies, respectively. The SP is poorly developed in the study formation (Table 2) and thus contributes little to discriminate diagenetic facies. Therefore, SP values were not used in this research.

Some diagenetic facies have similar log responses when discriminated by biplots of well logs, as shown in (Fig. 10). Though the plot of GR versus DEN is the best among bipolts of well logs to identify these facies, there is still about 55% overlap for identification sandstones with clay minerals cements (Table 3). One explanation is that two logs may not respond enough to petrographic characteristics to predict the diagenetic facies, thus more variables need to be added (Han et al., 2012). PCA as a data reduction procedure affords an excellent opportunity to synthesize well log variables to apply in discrimination of diagenetic facies (Han et al., 2012; Jolliffe, 2002). The performance result of PCA illustrates the prediction of diagenetic facies with all overlaps below 15% (Fig. 11A; Table 3).

Validation of the model

A blind test has been performed to evaluate the validation of the model in Cheng 96 well in Heshui Field, which is not used to build the model. Principal components are calculated (track 5 in Fig. 15) and diagenetic facies are predicted (track 6 in Fig. 15). The predicted diagenetic facies are corresponding with petrographic features of core samples, i.e. the predicted diagenetic facies are sandstones with dissolved unstable components, sandstones with carbonate cements, sandstones with clay minerals cements and tightly compacted sandstones at depths 1963.51 m, 1964.7 m, 1976.92 m and 1985.64 m respectively, and the photomicrographs at the same depths show petrography features which representing these diagenetic facies (Fig. 15). The successful application in Cheng 96 well suggests that the model can be used to predict diagenetic facies at a field-scale. This model may be not applicable in other basins or fields due to different sedimentary environment, provenance, tectonics and diagenetic history. Thus a significant future study would be validation of the model or at least the subgroup method of diagenetic facies and the prediction technique using principal components calculated by well logs in other basins or fields.

Conclusions

1. Sandstones in Chang 7 of the Heshui Field in Ordos Basin characterized by low porosity (av. 6.8%) and low permeability (av. 0.106×10^{-3} μm^2), which mainly results from intense mechanical compaction, cementation of clay minerals and carbonate, and dissolution of unstable components.

2. Mechanical compaction is far more important than cementation in porosity loss as COPL and CEPL are 28.6% and 10.7% respectively.

3. Secondary porosity from dissolved unstable components is not negligible as it constitutes up to 30% of total porosity and likely occurs in open systems.

4. Diagenetic facies can serve as a method to divide reservoirs into relatively homogeneous subgroups to facilitate reservoir evaluation. Sandstones with secondary porosity facies (i.e. sandstones with dissolved unstable components) show the best reservoir quality.

5. This study illustrates well logs are sensitive, to some degree, to various diagenetic alterations (e.g. compaction, carbonate cementation and dissolution), which thus indicate a good chance to upscale diagenetic facies with log properties to yield tools for prediction of reservoir quality.

6. Principal component analysis (PCA), rather than biplots of well logs, can be used as a helpful tool to build a model for diagenetic facies prediction. Application of the model using principal components in Cheng 96 well suggests the model could be applied at a field-scale.

7. A significant future study would be validation of the model or at least the subgroup

method of diagenetic facies and the prediction technique using principal component analysis (PCA) in other basins or fields.

Acknowledgements

This work was financially supported by the program of China Scholarship Council (No. 201506440024), National Natural Science Foundation of China (No. 41472115) and the National Science & Technology Major Project of China (No. 2016ZX05019005-007). Thanks are also given to PetroChina Changqing Oilfield Company for providing samples and data access and for permission to publish this work.

Reference

Amaefule, J.O., Altunbay, M., Tiab, D., Kersey, D.G., Keelan, D.K., 1993. Enhanced reservoir description: using core and log data to identify hydraulic (flow) units and predict permeability in uncored intervals/wells, SPE Annual Technical Conference and Exhibition. Society of Petroleum Engineers.

Boggs, S., Krinsley, D., 2006. Application of cathodoluminescence imaging to the study of sedimentary rocks. Cambridge University Press.

Bowman, M., 1998. Petroleum Geology of the North Sea, Basic Concepts and Recent Advances.

Chen, Y., Liu, Y., 1994. Diagenetic facies - a new approach to the prediction of reservoir rocks. Experimental Petroleum Geology 3.

Cosenza, P., Robinet, J., Pret, D., Huret, E., Fleury, M., Géraud, Y., Lebon, P., Villiéras, F., Zamora, M., 2014. Indirect estimation of the clay content of clay-rocks using acoustic measurements: New insights from the Montiers-sur-Saulx deep borehole (Meuse, France). Marine and Petroleum Geology 53, 117-132.

Duan, Y., 2012. Geochemical characteristics of crude oil in fluvial deposits from Maling oilfield of Ordos Basin, China. Organic geochemistry 52, 35-43.

Duan, Y., Wang, C., Zheng, C., Wu, B., Zheng, G., 2008. Geochemical study of crude oils from the Xifeng oilfield of the Ordos basin, China. Journal of Asian Earth Sciences 31, 341-356.

Folk, R.L., 1974. Petrology of sedimentary rocks. Hemphill Publishing Company.

Gluyas, J., Cade, C.A., 1997. Prediction of porosity in compacted sands. In: Kupecz, J.A., Gluyas, J., Bloch, S. (Eds.), Reservoir Quality Prediction in Sandstones and Carbonates. AAPG Mem. 69, 19-28.

Grigsby, J.D., Langford, R.P., 1996. Effects of diagenesis on enhanced-resolution bulk density logs in Tertiary Gulf Coast sandstones: An example from the Lower Vicksburg Formation, McAllen Ranch field, south Texas. AAPG bulletin 80, 1801-1819.

Guo, H., Jia, W., Peng, P.a., Lei, Y., Luo, X., Cheng, M., Wang, X., Zhang, L., Jiang, C., 2014. The

composition and its impact on the methane sorption of lacustrine shales from the Upper Triassic Yanchang Formation, Ordos Basin, China. Marine and Petroleum Geology 57, 509-520.
Han, X., Cui, Y., Li, F., Zhi, L., 2012. Classification and conventional logging identification of inhomogeneous reservoir in DB gas field. Progress in Geophysics 1, 186-192.
Henares, S., Caracciolo, L., Cultrone, G., Fernández, J., Viseras, C., 2014. The role of diagenesis and depositional facies on pore system evolution in a Triassic outcrop analogue (SE Spain). Marine and Petroleum Geology 51, 136-151.
Ji, L., Meng, F., Schiffbauer, J.D., Xu, J., Yan, K., Shu, J., 2008. Correlation between highly abundant oil-prone leiosphaerid acritarchs and hydrocarbon source rocks from the Triassic Yanchang Formation, eastern Gansu Province, Northwestern China. Gondwana Research 14, 554-560.
Jolliffe, I., 2002. Principal component analysis. Wiley Online Library.
Lai, J., Wang, G., Ran, Y., Zhou, Z., Cui, Y., 2016. Impact of diagenesis on the reservoir quality of tight oil sandstones: The case of Upper Triassic Yanchang Formation Chang 7 oil layers in Ordos Basin, China. Journal of Petroleum Science and Engineering 145, 54-65.
Liu, H., Zhao, Y., Luo, Y., Chen, Z., He, S., 2015. Diagenetic facies controls on pore structure and rock electrical parameters in tight gas sandstone. Journal of Geophysics and Engineering 12, 587-600.
Liu, Q., Chan, L., Liu, Q., Li, H., Wang, F., Zhang, S., Xia, X., Cheng, T., 2004. Relationship between magnetic anomalies and hydrocarbon microseepage above the Jingbian gas field, Ordos basin, China. AAPG bulletin 88, 241-251.
Lundegard, P., 1992. Sandstone porosity loss. A ‘‘big picture’’view of the importance of Compactation. J Sediment Petrol 62, 250-260.
Ma, S., Qi, Y., Zhang, X., Xia, Y., Song, C., Ma, L., Duan, Y., 2005. Geochemical characteristics and hydrocarbon generation potential of the source rocks in Yanchang Formation, Xifeng Oilfield, Ordos Basin, NW China. Petroleum Exploration & Development 32, 51-54.
Mansurbeg, H., De Ros, L., Morad, S., Ketzer, J., El-Ghali, M., Caja, M., Othman, R., 2012. Meteoric-water diagenesis in late Cretaceous canyon-fill turbidite reservoirs from the Espírito Santo Basin, eastern Brazil. Marine and Petroleum Geology 37, 7-26.
Morad, S., Al-Ramadan, K., Ketzer, J.M., De Ros, L., 2010. The impact of diagenesis on the heterogeneity of sandstone reservoirs: A review of the role of depositional facies and sequence stratigraphy. AAPG bulletin 94, 1267-1309.
Nguyen, B.T., Jones, S.J., Goulty, N.R., Middleton, A.J., Grant, N., Ferguson, A., Bowen, L., 2013. The role of fluid pressure and diagenetic cements for porosity preservation in Triassic fluvial reservoirs of the Central Graben, North Sea. AAPG bulletin 97, 1273-1302.
Niu, X., Feng, S., Liu, F., 2013. Microscopic occurrence of oil in tight sandstones and its relation with oil sources: A case study from the Upper Triassic Yanchang formation, Ordos basin. Oil & Gas Geology 34, 288-293.
Ozkan, A., Cumella, S.P., Milliken, K.L., Laubach, S.E., 2011. Prediction of lithofacies and reservoir quality using well logs, late cretaceous williams fork formation, mamm creek field, piceance basin, colorado. AAPG bulletin 95, 1699-1723.
Paxton, S., Szabo, J., Ajdukiewicz, J., Klimentidis, R., 2002. Construction of an intergranular volume compaction curve for evaluating and predicting compaction and porosity loss in rigid-grain sandstone reservoirs. AAPG bulletin 86, 2047-2067.
Perez, H.H., Datta-Gupta, A., Mishra, S., 2005. The role of electrofacies, lithofacies, and hydraulic flow units in permeability predictions from well logs: a comparative analysis using classification trees.

SPE Reservoir Evaluation & Engineering 8, 143-155.
Porras, J., Barbato, R., Khazen, L., 1999. Reservoir flow units: a comparison between three different models in the Santa Barbara and Pirital fields, North Monagas area, Eastern Venezuela Basin, Latin American and Caribbean Petroleum Engineering Conference. Society of Petroleum Engineers.
Qiu, X., Liu, C., Mao, G., Deng, Y., Wang, F., Wang, J., 2014. Late Triassic tuff intervals in the Ordos basin, Central China: Their depositional, petrographic, geochemical characteristics and regional implications. Journal of Asian Earth Sciences 80, 148-160.
Qiu, X., Liu, C., Wang, F., Deng, Y., Mao, G., 2015. Trace and rare earth element geochemistry of the Upper Triassic mudstones in the southern Ordos Basin, Central China. Geological Journal 50, 399-413.
Ren, Z., Li, W., Yu, L., Wu, X., Qiang, Y., Long, R., Wei, W., 2014. Tight oil reservoir formation conditions and main controlling factors of Yanchang Formation in southeastern Ordos Basin. Oil & Gas Geology 35, 190-198.
Rossi, C., Alaminos, A., 2014. Evaluating the mechanical compaction of quartzarenites: The importance of sorting (Llanos foreland basin, Colombia). Marine & Petroleum Geology 56, 222-238.
Rushing, J.A., Newsham, K.E., Blasingame, T.A., 2008. Rock typing: Keys to understanding productivity in tight gas sands, SPE Unconventional Reservoirs Conference. Society of Petroleum Engineers.
Salem, A.M., Morad, S., Mato, L.F., Al-Aasm, I., 2000. Diagenesis and reservoir-quality evolution of fluvial sandstones during progressive burial and uplift: Evidence from the Upper Jurassic Boipeba Member, Reconcavo Basin, Northeastern Brazil. AAPG bulletin 84, 1015-1040.
Salomons, W., Goudie, A., Mook, W., 1978. Isotopic composition of calcrete deposits from Europe, Africa and India. Earth Surface Processes 3, 43-57.
Selley, R., 1992. The third age of wireline log analysis: Application to reservoir diagenesis. Geological Society, London, Special Publications 65, 377-387.
Serra, O., 1984. Fundamentals of Well-Log Interpretation (Vol 1): The Acquisition of Logging Data (Developments in Petroleum Science A15). Amsterdam: Elsevier.
Serra, O., 1986. Fundamentals of well-log interpretation-2. The interpretation of logging data, developments in petroleum science (15B). Fundamentals of well-log interpretation-2. The interpretation of logging data, developments in petroleum science (15B).
Shi, J., Wang, J., Mao, M., Wang, Q., Guo, Z., Guo, X., Lu, L., 2003. Reservoir sandstone diagenesis of memeber 6 to 8 in Yanchang formation (Triassic), Xifeng Oilfield, Ordos Basin. Acta Sedimentologica Sinica 21, 373-380.
Stricker, S., Jones, S.J., Grant, N.T., 2016a. Importance of vertical effective stress for reservoir quality in the Skagerrak Formation, Central Graben, North Sea. Marine and Petroleum Geology.
Stricker, S., Jones, S.J., Sathar, S., Bowen, L., Oxtoby, N., 2016b. Exceptional reservoir quality in HPHT reservoir settings: examples from the Skagerrak Formation of the Heron Cluster, UK, North Sea. Marine and Petroleum Geology.
Taylor, T.R., Giles, M.R., Hathon, L.A., Diggs, T.N., Braunsdorf, N.R., Birbiglia, G.V., Kittridge, M.G., Macaulay, C.I., Espejo, I.S., 2010. Sandstone diagenesis and reservoir quality prediction: Models, myths, and reality. AAPG Bulletin 94, 1093-1132.
Vermeesch, P., 2012. On the visualisation of detrital age distributions. Chemical Geology 312–313, 190-194.
Wang, J., Cao, Y., Liu, K., Liu, J., Xue, X., Xu, Q., 2016. Pore fluid evolution, distribution and water-rock interactions of carbonate cements in red-bed sandstone reservoirs in the Dongying

Depression, China. Marine and Petroleum Geology 72, 279-294.
Xi, K., Cao, Y., Jahren, J., Zhu, R., Bjørlykke, K., Haile, B.G., Zheng, L., Hellevang, H., 2015. Diagenesis and reservoir quality of the Lower Cretaceous Quantou Formation tight sandstones in the southern Songliao Basin, China. Sedimentary Geology 330, 90-107.
Xi, S., Li, W., Li, R., 2008. Hydrocarbon generation and reservoir formation: A case from Chang 7 source rock in Majiatan area, west margin of Ordos Basin. Petroleum Exploration and Development 35, 657-663.
Xinquan, R., Shenghe, W., Jing, F., 2013. Research on the pore structure classification of low permeability reservoir of the Yanchang Formation in Longdong Area, Ordos Basin. Earth Science Frontiers 20, 77-85.
Yang, H., Deng, X., 2013. Deposition of Yanchang Formation deep-water sandstone under the control of tectonic events in the Ordos Basin. Petroleum Exploration and Development 40, 549-557.
Yang, H., Dou, W., Liu, X., Zhang, C., 2010. Analysis on sedimentary facies of member 7 in Yanchang formation of Triassic in Ordos Basin. Acta Sedimentologica Sinica 28, 254-263.
Yuan, G., Cao, Y., Gluyas, J., Li, X., Xi, K., Wang, Y., Jia, Z., Sun, P., Oxtoby, N.H., 2015. Feldspar dissolution, authigenic clays, and quartz cements in open and closed sandstone geochemical systems during diagenesis: Typical examples from two sags in Bohai Bay Basin, East China. AAPG Bulletin 99, 2121-2154.
Zeng, L., Li, X., 2009. Fractures in sandstone reservoirs with ultra-low permeability: A case study of the Upper Triassic Yanchang Formation in the Ordos Basin, China. AAPG bulletin 93, 461-477.
Zhang, W., Yang, H., Hou, L., Liu, F., 2009. Distribution and geological significance of 17α (H)-diahopanes from different hydrocarbon source rocks of Yanchang Formation in Ordos Basin. Science in China Series D: Earth Sciences 52, 965-974.
Zhao, J., Mountney, N.P., Liu, C., Qu, H., Lin, J., 2015. Outcrop architecture of a fluvio-lacustrine succession: Upper Triassic Yanchang Formation, Ordos Basin, China. Marine and Petroleum Geology 68, 394-413.
Zhao, M.-W., Behr, H.-J., Ahrendt, H., Wemmer, K., Ren, Z.-L., Zhao, Z.-Y., 1996. Thermal and tectonic history of the Ordos Basin, China: Evidence from apatite fission track analysis, vitrinite reflectance, and K-Ar dating. AAPG bulletin 80, 1110-1133.
Zhong, D., Zhou, L., Sun, H., Yao, J., Liu, X., Luo, A., Deng, X., 2013. Petrology of sandstone reservoirs in Longdong Area, Ordos Basin. Earth Science Frontiers 20, 52-60.
Zhu, H., Chen, K., Liu, K., He, S., 2008. A sequence stratigraphic model for reservoir sand-body distribution in the Lower Permian Shanxi Formation in the Ordos Basin, northern China. Marine and Petroleum Geology 25, 731-743.
Zou, C., Tao, S., Zhou, H., Zhang, X., He, D., Zhou, C., Wang, L., Wang, X., Li, F., Zhu, R., 2008. Genesis, classification, and evaluation method of diagenetic facies. Petroleum Exploration and Development 35, 526-540.
Zou, C., Wang, L., Li, Y., Tao, S., Hou, L., 2012. Deep-lacustrine transformation of sandy debrites into turbidites, Upper Triassic, Central China. Sedimentary Geology 265, 143-155.

Figures

Figure 1 Map showing locations of A) Ordos Basin in north central China, and B) Heshui Field; C) Geological cross section of line AA' in B), modified from Zhao et al. (2015); D) wells in this study. The well with red colour is Cheng 96, which is used for validating the model in this article.

Figure 2 Triassic stratigraphy of Yanchang formation, showing an overall record of palaeo-lake deposits.

Figure 3 Ternary diagram of framework grains composition in Chang 7 unit, Heshui Field.

Figure 4 Core sample photographs. A) Fine-grained sandstones with parallel bedding, well Zhuang 42, 1843.4 m; B) Fine-grained sandstones with subrounded mud pebbles, well Zhuang 42, 1846.4 m; C) Fine-grained sandstones with parallel bedding and flame structure, well Zhuang 215, 1860.4 m; D) Fine-grained sandstones with massive bedding, well Zhuang 158, 1729.8 m; E) Siltstones with black carbonized plants, well Zhuang 226, 1735.5 m; F) Fine-grained sandstones with convolute bedding, well Zhuang 226, 1710.05 m.

Figure 5 Plot of porosity versus permeability, showing most core samples with porosity below 10% and permeability below $1\times10^{-3}\mu m^2$, and poor or no correlation between porosity and permeability (R^2=0.39).

Figure 6 Optical photomicrographs and SEM images showing: A) Plane-polarized light (PPL) view of primary intergranular pores, secondary intragranular pores and presence of grain-coating chlorite; well Zhuang 205 1814.93 m; B) Plane-polarized light view of primary intergranular pores, secondary intragranular pores and existence of carbonate cements and clay minerals; well Zhuang 189, 1546.11 m; C) SEM image of pores with pore-bridging illite and grain-coating chlorite; well Zhuang 23, 1900.14 m; D) SEM image of occurrence of a micro-fracture; well Cheng 96, 1992.29 m.

Figure 7 Optical photomicrographs and SEM images showing A) Quartz overgrowths occupy much intergranular volume; PPL, well Zhuang 120, 1736.8 m; B) The euhedral quartz crystal occurs in secondary pores resulting from feldspar dissolution; SEM, well Zhuang 205, 1816.65 m; C) Sandstones cemented with pervasive poikilitic calcite show little remnant intergranular pore space; PPL, well Zhuang 191,

1185.39 m; D) Dolomite and calcite cements occlude intergranular pores; cathodoluminescence (CL), well Zhuang 240, 1785.6 m; E) Euhedral massive ferroan calcite; SEM, well Zhuang 58, 2163.33 m; F) Ankerite occur mainly as a intergranular cement, and minor amount of ankerite occur in secondary pores; PPL, well Zhuang 21, 1212.50 m; G) Intergranular bridging illite and I/S mixed layer destroy pores connection; SEM, well Zhuang 126, 1628.25 m; H) Chlortie occur as grain coats and pore-filling cement; SEM, well Zhuang 81, 1924.3 m; I) Grain-replacive kaolinite, well Zhuang 14, 1713.96 m; J) Concave-convex grain contacts indicate intense compaction; PPL, well Zhuang 177, 1902.6 m; K) PPL view of secondary pores caused by part to entire grain dissolution; well Zhuang 57, 2102.8 m; L) SEM image of remnant of feldspars resulting from dissolution; well Zhuang 40, 1817.85 m.

Figure 8 Plot of compactional porosity loss (COPL) versus cementational porosity loss (CEPL) with remaining intergranular porosity (dashed lines).

Figure 9 Photomicrographs of four diagenetic facies. A) Sandstones with dissolved unstable components, in which secondary pores are common and have enhanced reservoir quality; PPL, well Zhuang 21, 1440 m; B) Sandstones with clay minerals cements, in which clay minerals tend to occlude intergranular pores; well Zhuang 140, 1837.96 m; C) Sandstones with carbonate cements, in which poikilotopic carbonate cements occupy most intergranular volume; PPL, well Zhuang 232, 1768.77 m; D) Tightly compacted sandstones/siltstones, in which grains show similar orientations; PPL, well Zhuang 8, 1589.0 m.

Figure 10 Crossplots of gamma ray (GR) versus A) bulk density; B) borehole-compensated sonic (AC); C) thermal neutron porosity (CNL) and D) deep resistivity (RT). These crossplots show tightly compacted sandstones/siltstones are easily to be identified with high GR values, and sandstones with dissolved unstable components can also be distinguished with low DEN values. However, there is still much overlap in the crossplot of GR versus DEN, which has the lowest overlap in these crossplots.

Figure 11 Crossplots of principal components distinguishing diagenetic facies. A) Crossplot P1 versus P2 shows obvious respective regions for these diagenetic facies; B) Crossplot P1 versus P3 indicates, on the contrary, much overlap as similar P3 ranges in these diagenetic facies. See Figure 10 for legends.

Figure 12 Paragenetic sequence of the diagenetic processes modified from Lai et al. (2016), Ren et al. (2014) and Shi et al. (2003).

Figure 13 Plots of A) porosity and B) permeability versus secondary porosity, carbonate cements, quartz cement, total clay minerals and chlorite. Secondary porosity shows obvious positive relationships with porosity and permeability. Whereas both carbonate cements and clay minerals indicate negative relationships with porosity and permeability. For quartz cement, the relationships with porosity and permeability are very weak. See text for more details.

Figure 14 Porosity versus permeability with various diagenetic facies Sandstones with dissolved unstable components show best reservoir quality, whereas tightly compacted sandstones/siltstones have poorest reservoir quality. See Figure 10 for legends and see text for details.

Figure 15 Prediction of diagenetic facies in Cheng 96 well to validate the model. The diagenetic facies (track 6) predicted based on principal components (i.e. P1 and P2; track 5) calculated by well logs are correspondent with petrographic characteristics of rock samples (track 7).

Tables

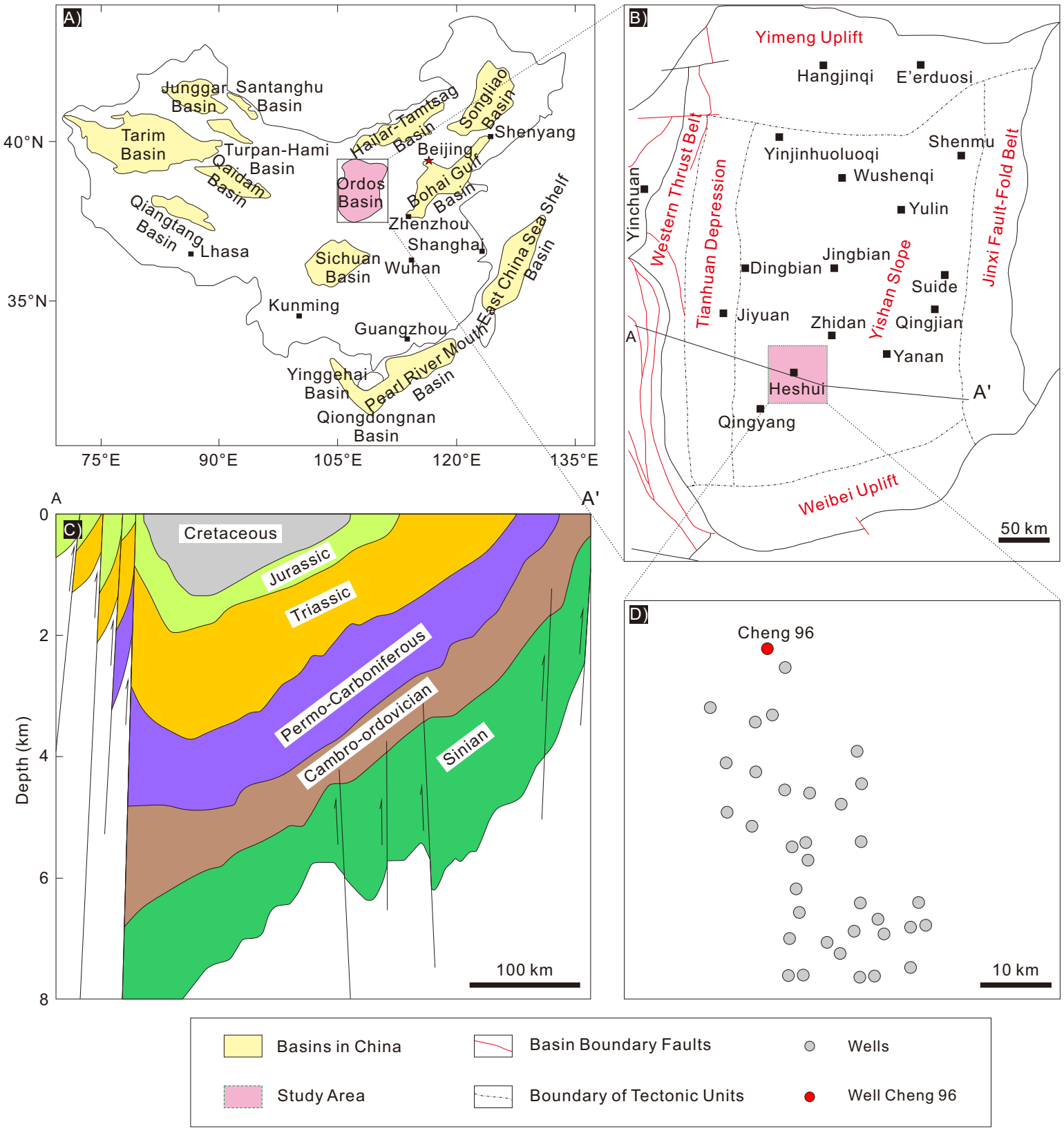
A)
Junggar Basin
Santanghu Basin
Tarim Basin
Turpan-Hami Basin
Qaidam Basin
Qiangtang Basin
Lhasa
Ordos Basin
Hailar-Tamtsag Basin
Songliao Basin
Shenyang
Beijing
Bohai Gulf Basin
Zhenzhou
Shanghai
Sichuan Basin
Wuhan
East China Sea Shelf Basin
Kunming
Guangzhou
Pearl River Mouth Basin
Yinggehai Basin
Qiongdongnan Basin
40°N
35°N
75°E
90°E
105°E
120°E
135°E
B)
Yimeng Uplift
Hangjinqi
E'erduosi
Yinjinhuoluoqi
Shenmu
Wushenqi
Yulin
Yinchuan
Western Thrust Belt
Tianhuan Depression
Jinxi Fault-Fold Belt
Jingbian
Dingbian
Yishan Slope
Suide
Jiyuan
Zhidan
Qingjian
Yanan
Heshui
Qingyang
Weibei Uplift
50 km
C)
Cretaceous
Jurassic
Triassic
Permo-Carboniferous
Cambro-ordovician
Sinian
Depth (km)
100 km
D)
Cheng 96
10 km
Basins in China
Study Area
Basin Boundary Faults
Boundary of Tectonic Units
Wells
Well Cheng 96

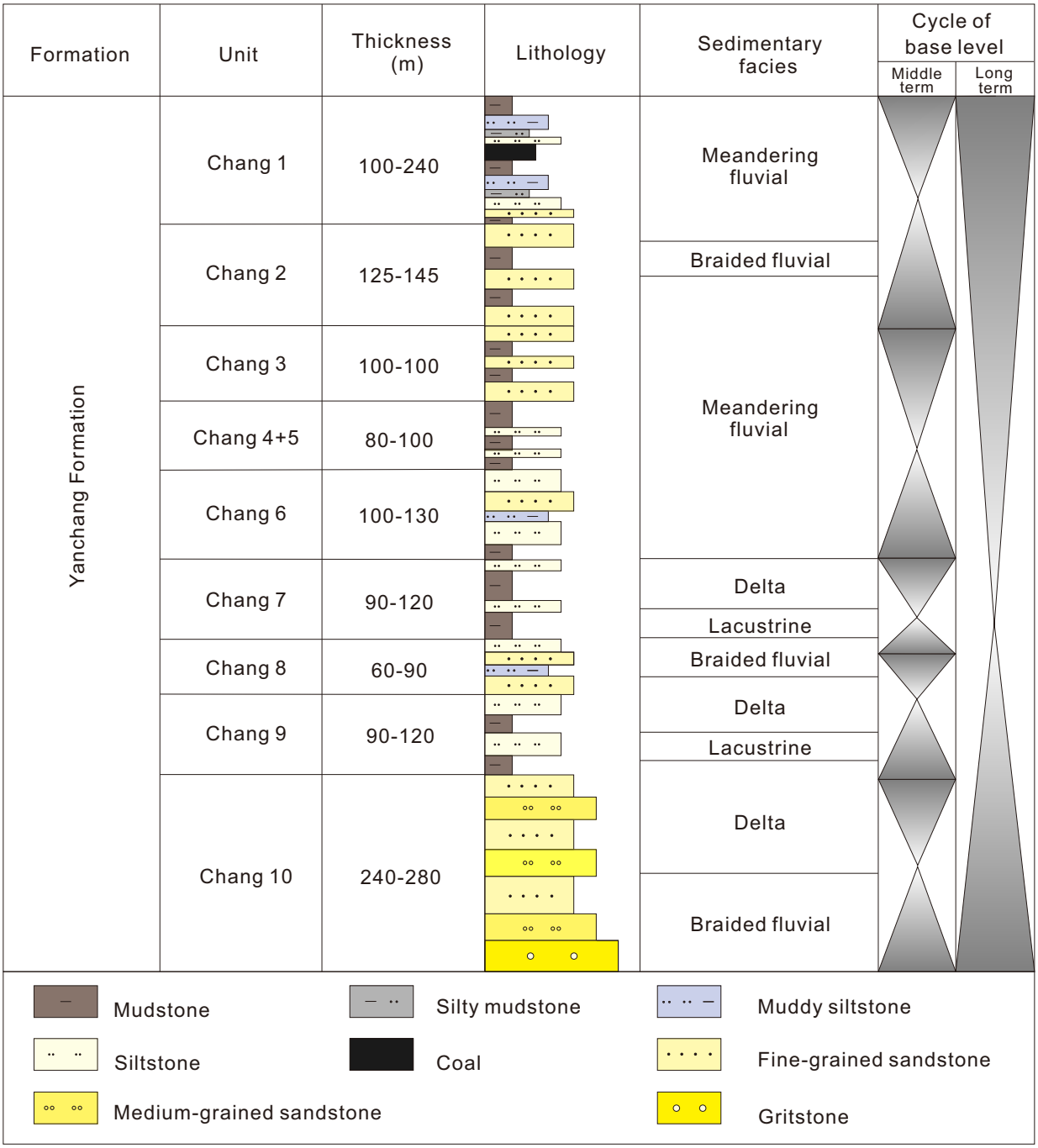
Formation
Unit
Thickness (m)
Lithology
Sedimentary facies
Cycle of base level
Middle term
Long term
Yanchang Formation
Chang 1
100-240
Meandering fluvial
Chang 2
125-145
Braided fluvial
Chang 3
100-100
Meandering fluvial
Chang 4+5
80-100
Chang 6
100-130
Chang 7
90-120
Delta
Lacustrine
Chang 8
60-90
Braided fluvial
Chang 9
90-120
Delta
Lacustrine
Chang 10
240-280
Delta
Braided fluvial
Mudstone
Silty mudstone
Muddy siltstone
Siltstone
Coal
Fine-grained sandstone
Medium-grained sandstone
Gritstone

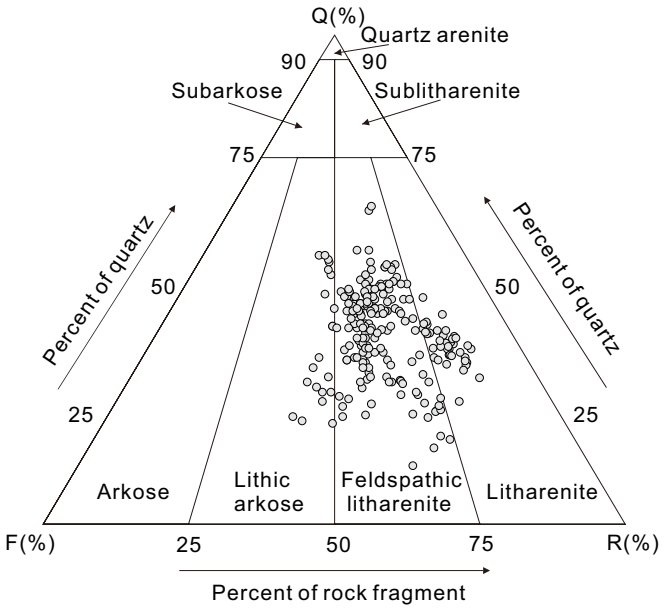
Q(%)
Quartz arenite
90
90
Subarkose
Sublitharenite
75
75
Percent of quartz
50
50
Percent of quartz
25
25
Arkose
Lithic
arkose
Feldspathic
litharenite
Litharenite
F(%)
25
50
75
R(%)
Percent of rock fragment

A)

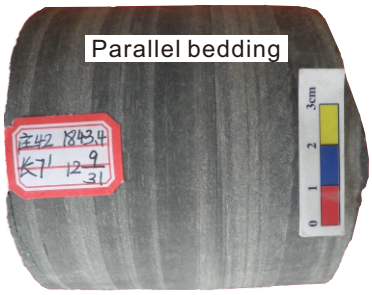
Parallel bedding

B)

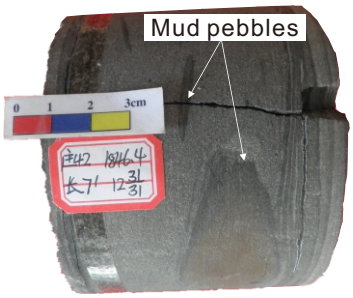
Mud pebbles

C)

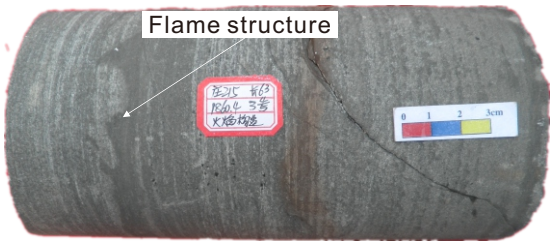
Flame structure

D)


Massive bedding

E)

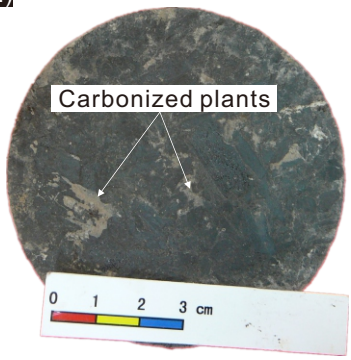
Carbonized plants
0 1 2 3 cm

F)

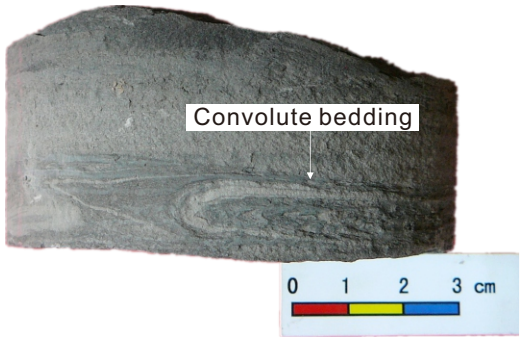
Convolute bedding
0 1 2 3 cm

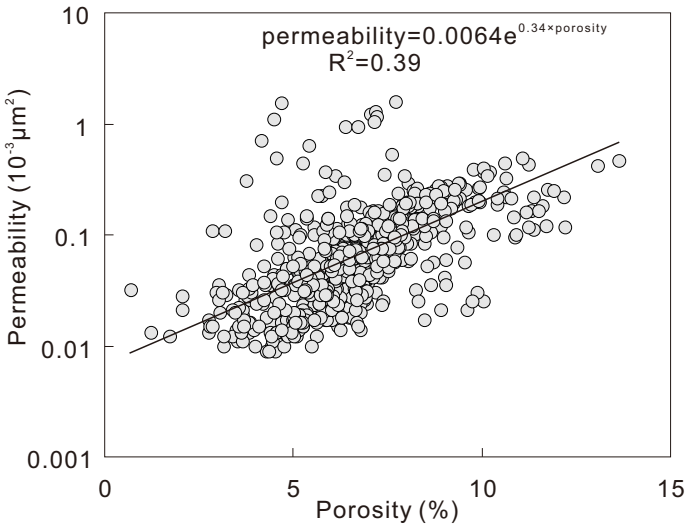
permeability=0.0064e^0.34×porosity
R^2=0.39
Permeability (10^-3 μm^2)
10
1
0.1
0.01
0.001
0
5
10
15
Porosity (%)

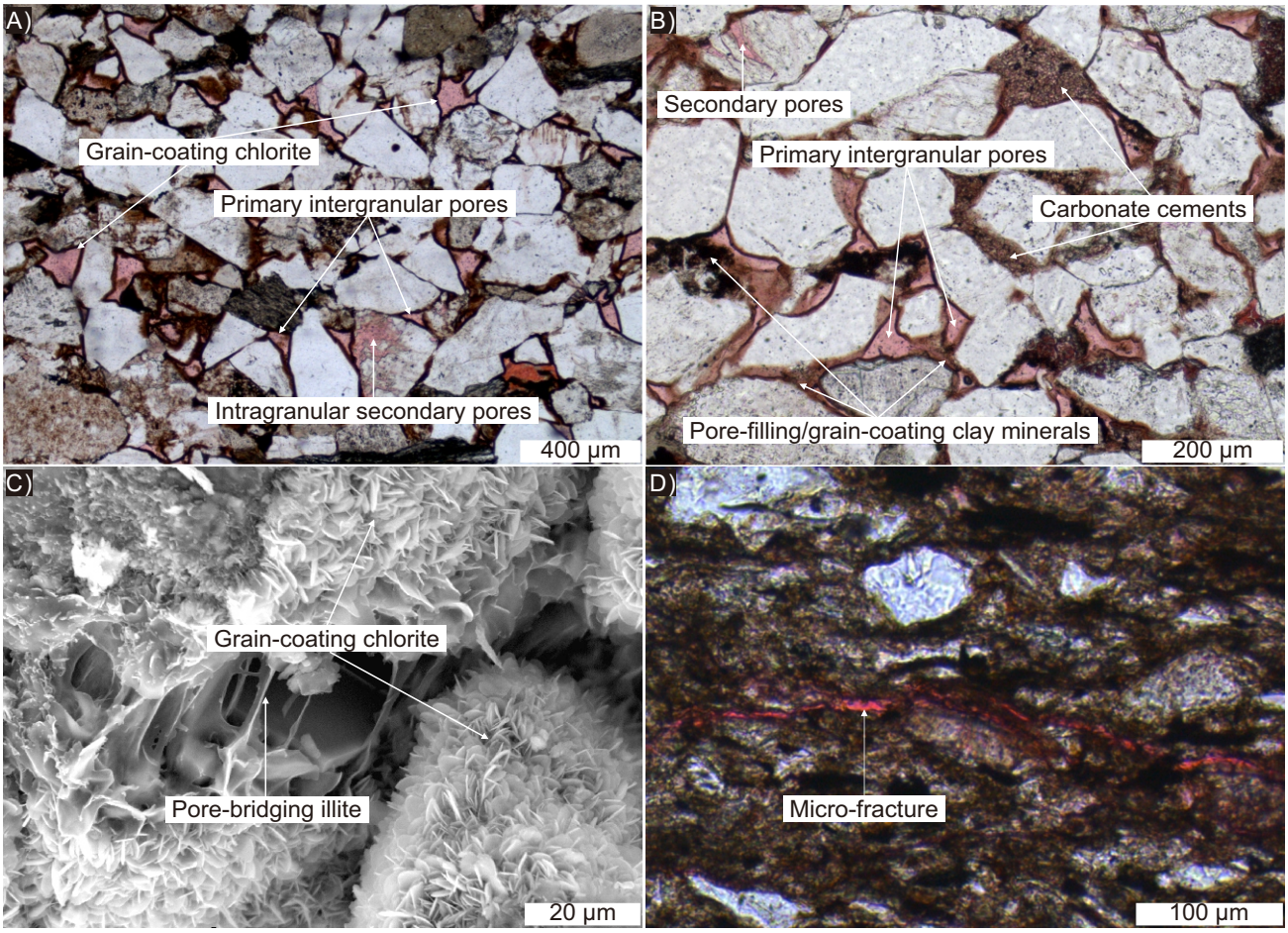
A)
Grain-coating chlorite
Primary intergranular pores
Intragranular secondary pores
400 μm
B)
Secondary pores
Primary intergranular pores
Carbonate cements
Pore-filling/grain-coating clay minerals
200 μm
C)
Grain-coating chlorite
Pore-bridging illite
20 μm
D)
Micro-fracture
100 μm

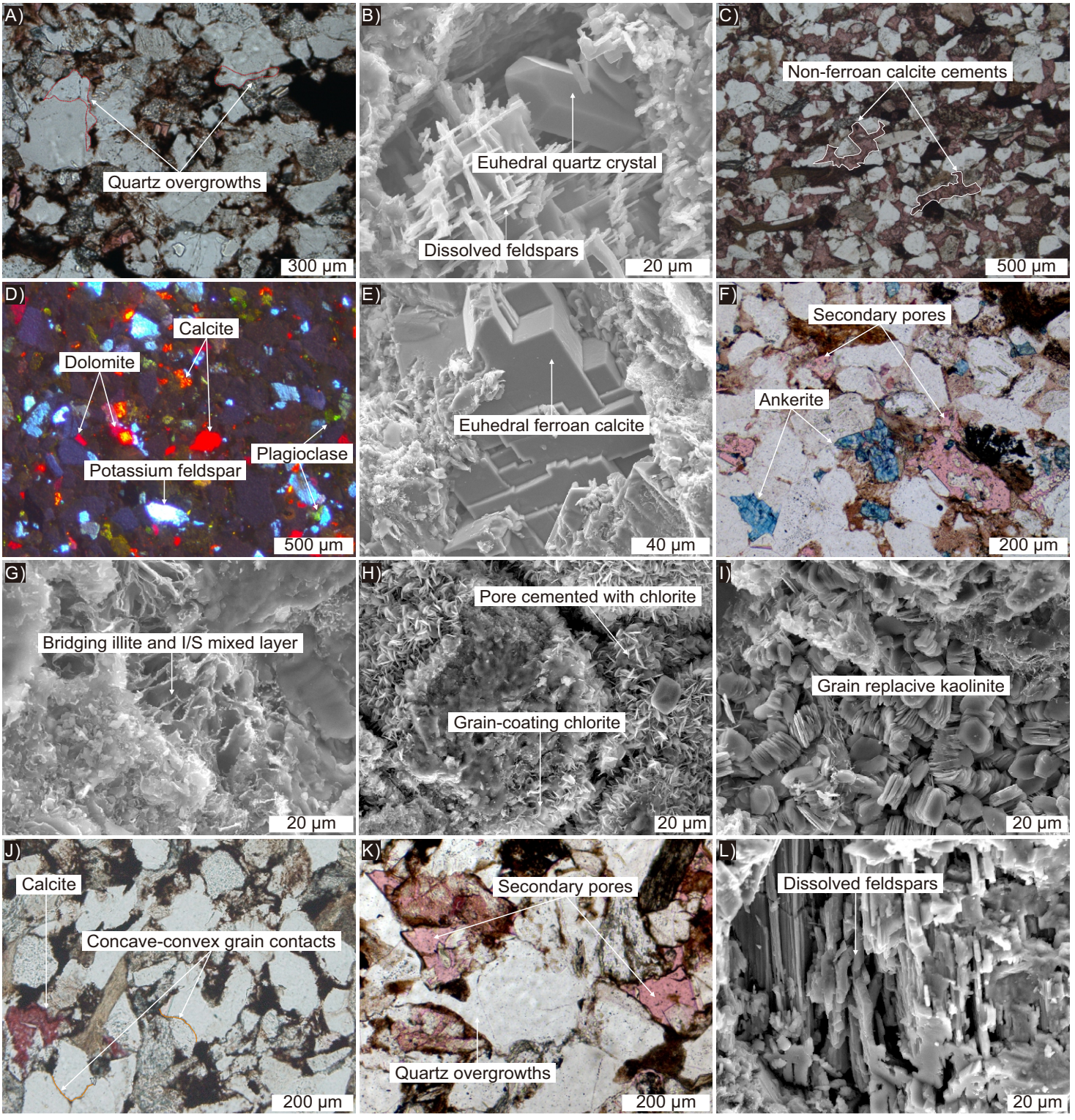
A)
Quartz overgrowths
300 μm
B)
Euhedral quartz crystal
Dissolved feldspars
20 μm
C)
Non-ferroan calcite cements
500 μm
D)
Calcite
Dolomite
Plagioclase
Potassium feldspar
500 μm
E)
Euhedral ferroan calcite
40 μm
F)
Secondary pores
Ankerite
200 μm
G)
Bridging illite and I/S mixed layer
20 μm
H)
Pore cemented with chlorite
Grain-coating chlorite
20 μm
I)
Grain replacive kaolinite
20 μm
J)
Calcite
Concave-convex grain contacts
200 μm
K)
Secondary pores
Quartz overgrowths
200 μm
L)
Dissolved feldspars
20 μm

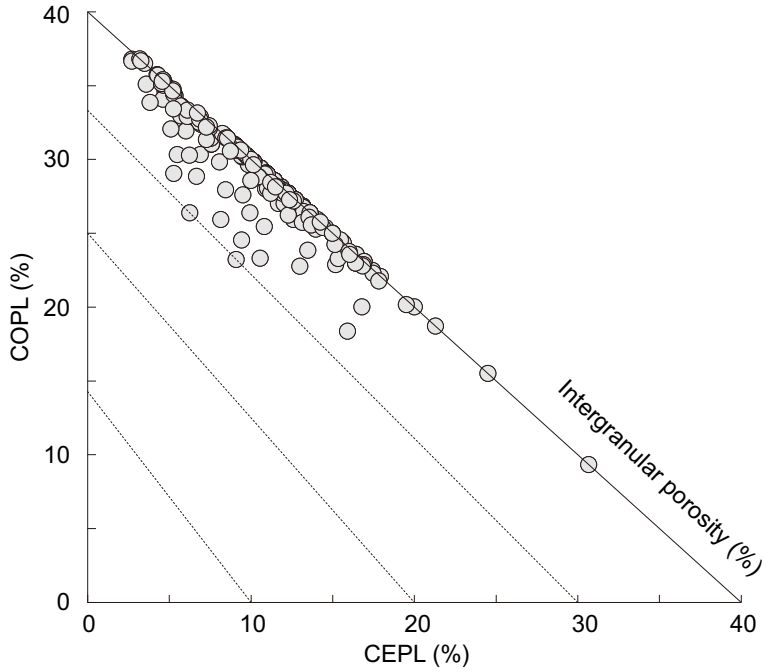
40
30
20
10
0
COPL (%)
0
10
20
30
40
CEPL (%)
Intergranular porosity (%)

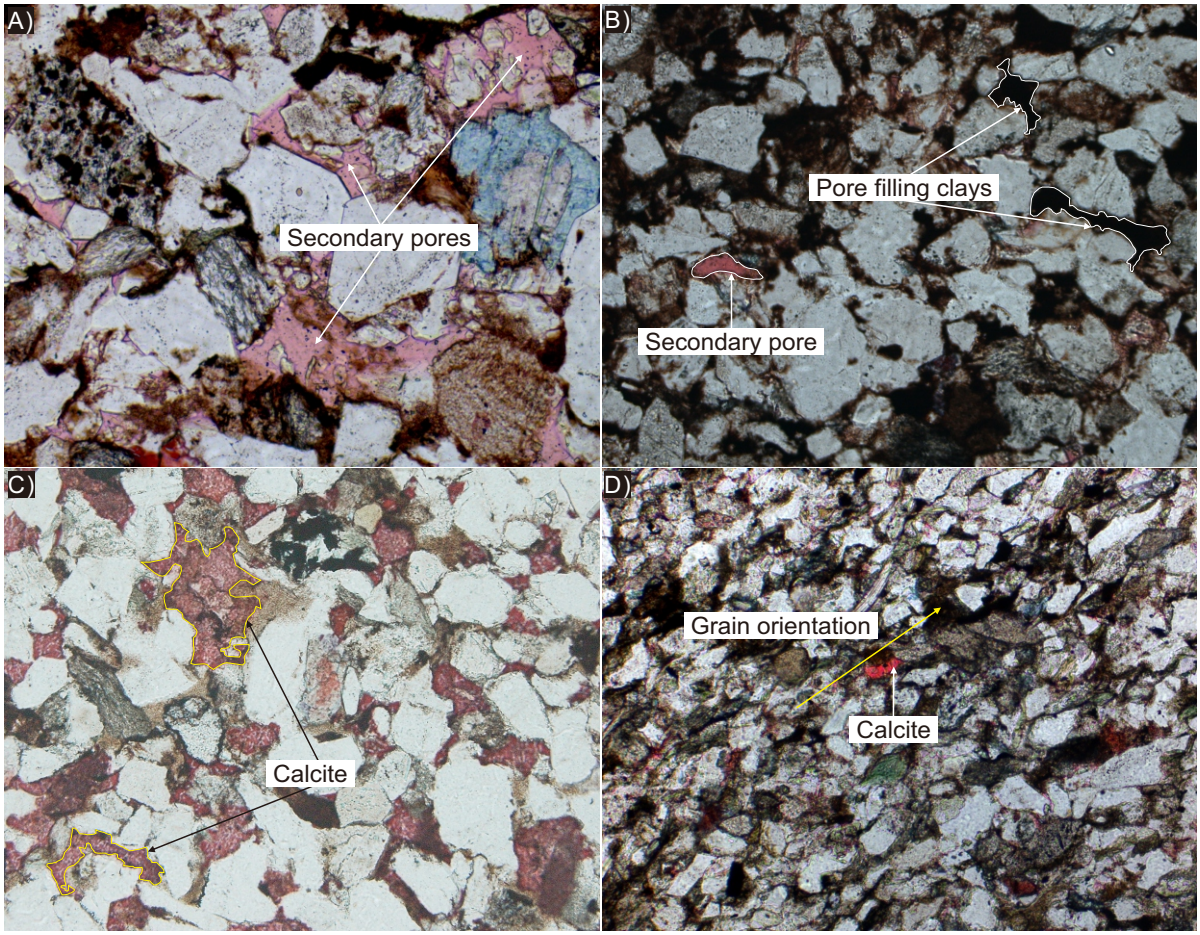
A)
Secondary pores
B)
Pore filling clays
Secondary pore
C)
Calcite
D)
Grain orientation
Calcite

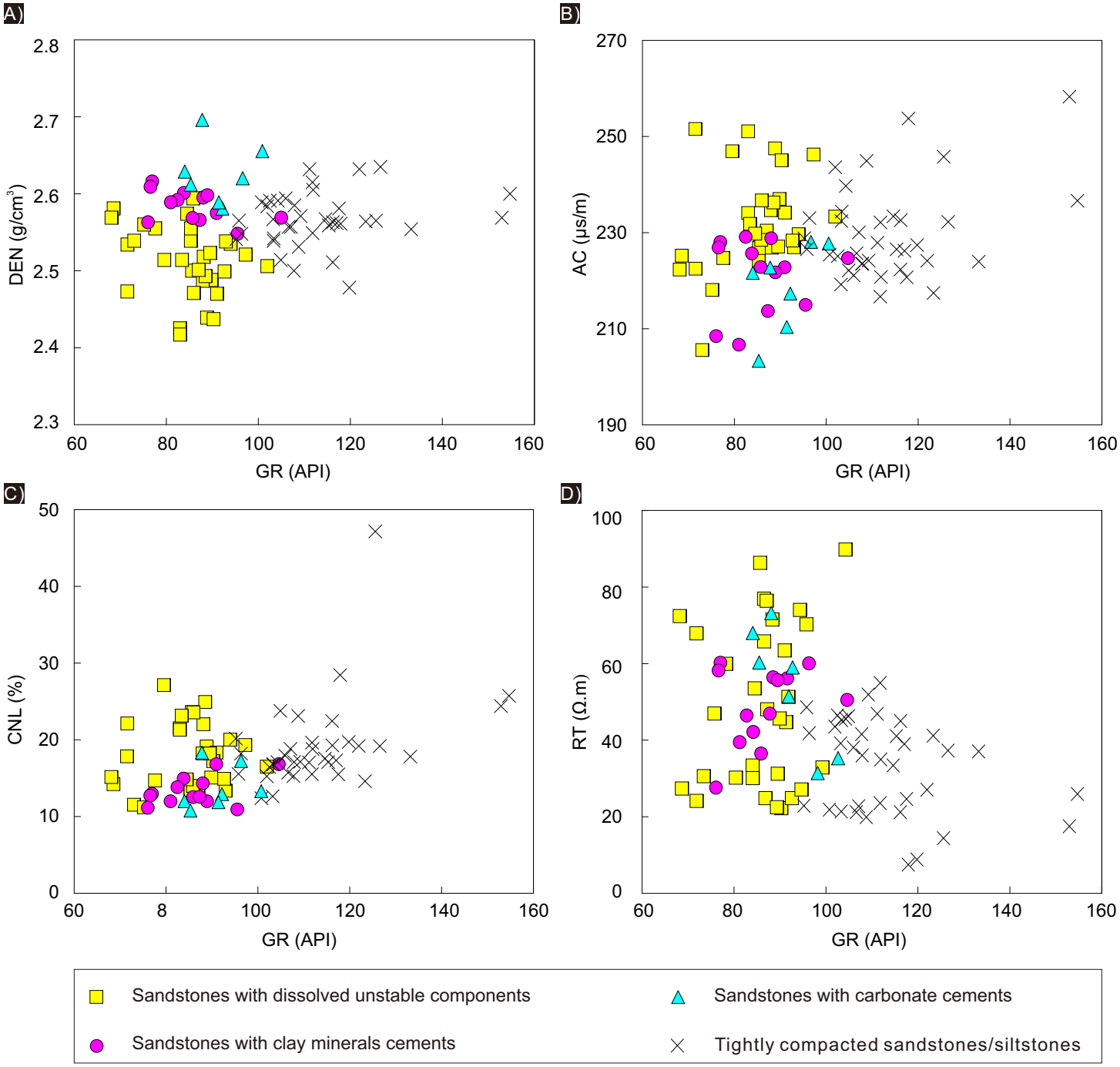
A)
DEN (g/cm3)
2.8
2.7
2.6
2.5
2.4
2.3
60
80
100
120
140
160
GR (API)
B)
AC (μs/m)
270
250
230
210
190
60
80
100
120
140
160
GR (API)
C)
CNL (%)
50
40
30
20
10
0
60
8
100
120
140
160
GR (API)
D)
RT (Ω.m)
100
80
60
40
20
0
60
80
100
120
140
160
GR (API)
Sandstones with dissolved unstable components
Sandstones with carbonate cements
Sandstones with clay minerals cements
Tightly compacted sandstones/siltstones

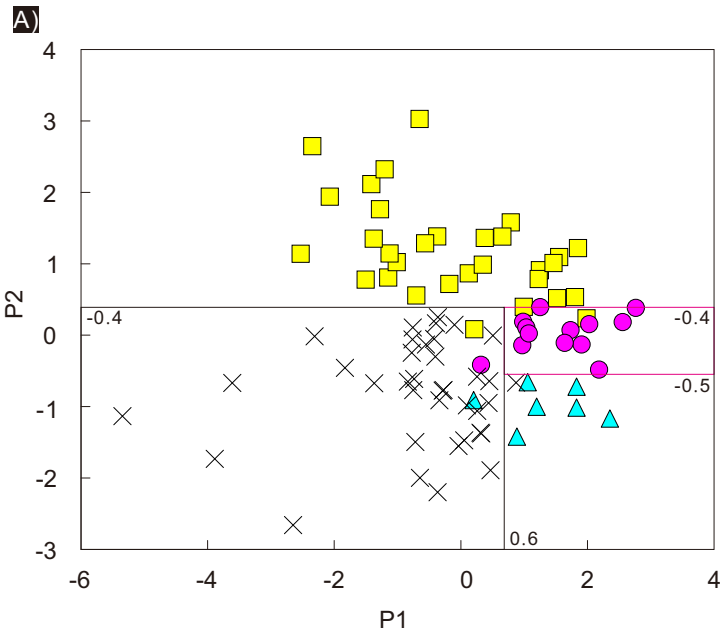
A)
P2
P1
-0.4
-0.4
-0.5
0.6

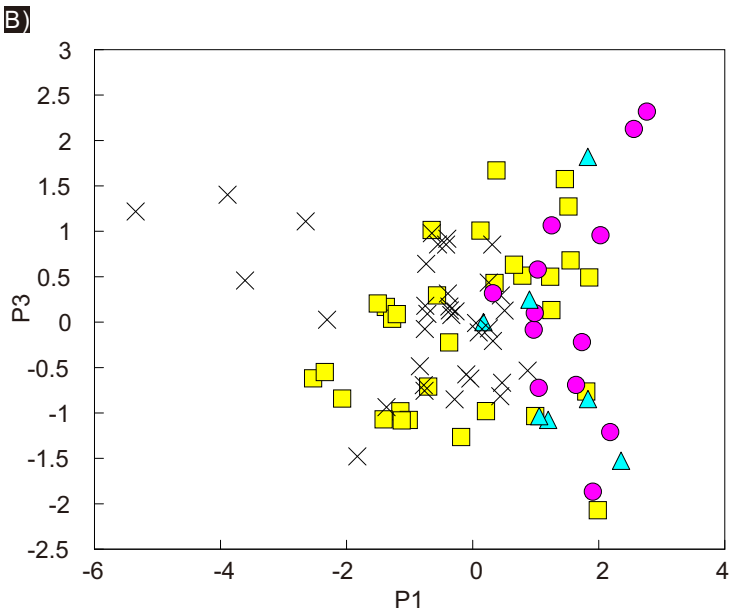
B)
P3
P1

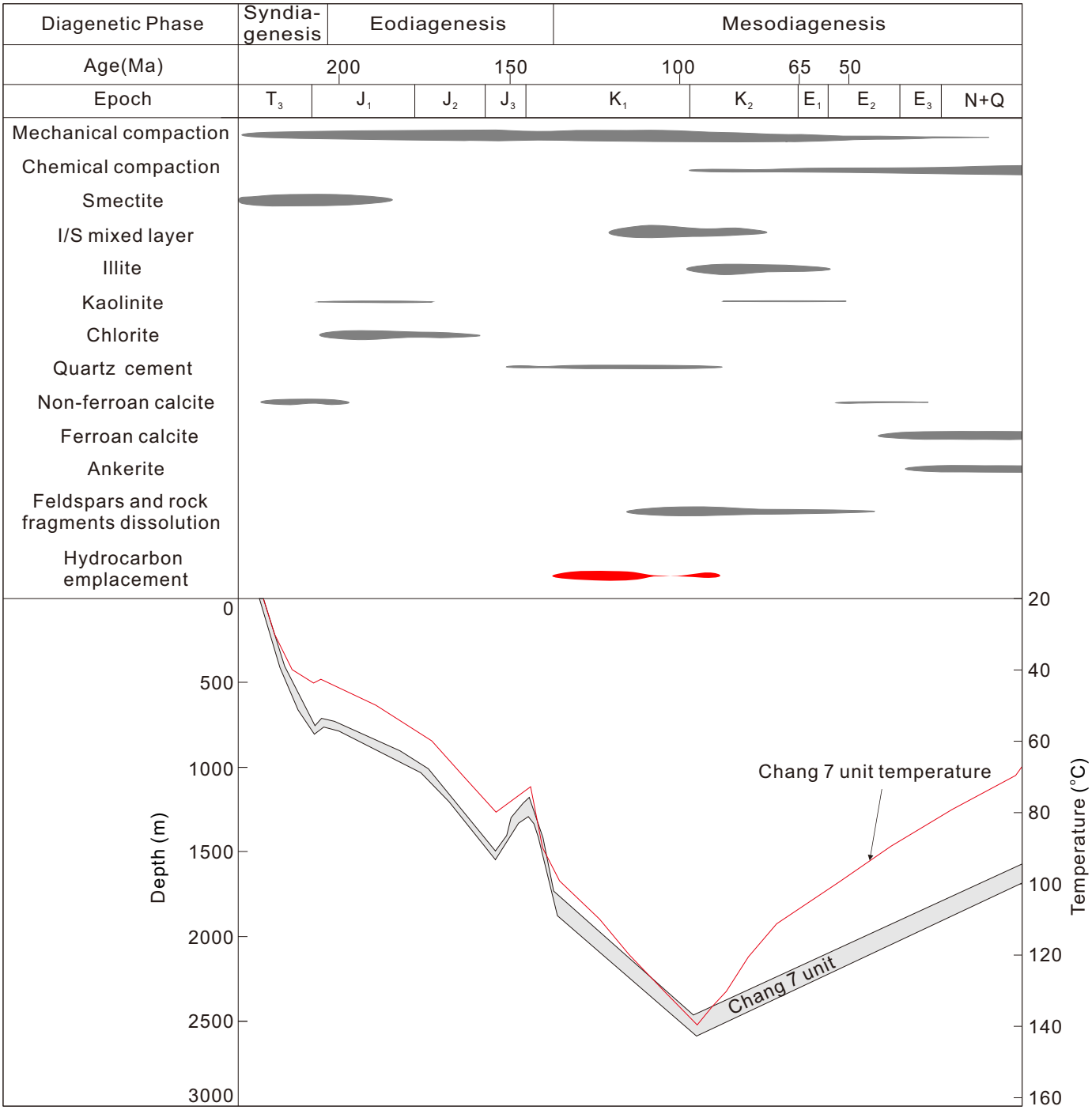
Diagenetic Phase
Syndia-genesis
Eodiagenesis
Mesodiagenesis
Age(Ma)
200
150
100
65
50
Epoch
T3
J1
J2
J3
K1
K2
E1
E2
E3
N+Q
Mechanical compaction
Chemical compaction
Smectite
I/S mixed layer
Illite
Kaolinite
Chlorite
Quartz cement
Non-ferroan calcite
Ferroan calcite
Ankerite
Feldspars and rock fragments dissolution
Hydrocarbon emplacement
Depth (m)
0
500
1000
1500
2000
2500
3000
Chang 7 unit temperature
Chang 7 unit
Temperature (°C)
20
40
60
80
100
120
140
160

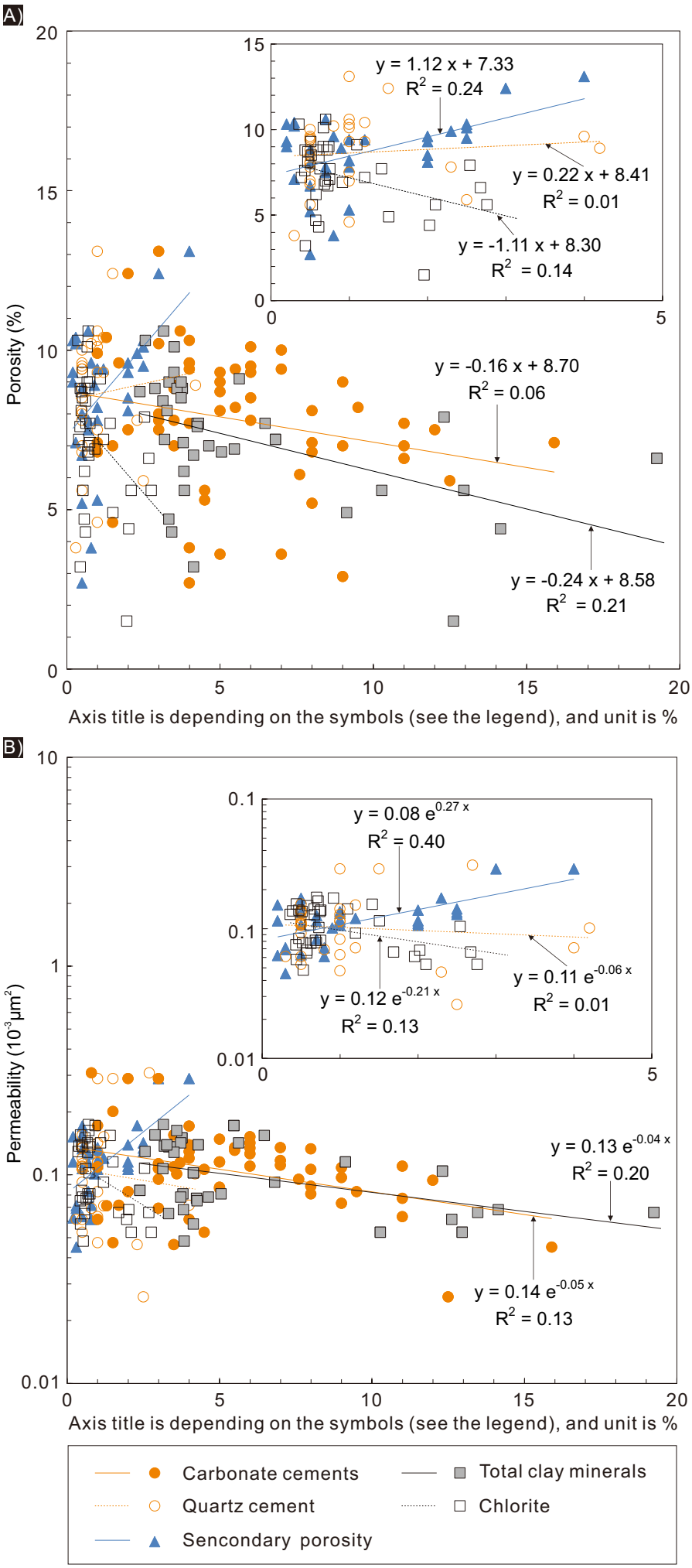
A)
Porosity (%)
y = 1.12 x + 7.33
R2 = 0.24
y = 0.22 x + 8.41
R2 = 0.01
y = -1.11 x + 8.30
R2 = 0.14
y = -0.16 x + 8.70
R2 = 0.06
y = -0.24 x + 8.58
R2 = 0.21
Axis title is depending on the symbols (see the legend), and unit is %
B)
Permeability (10-3μm2)
y = 0.08 e0.27 x
R2 = 0.40
y = 0.11 e-0.06 x
R2 = 0.01
y = 0.12 e-0.21 x
R2 = 0.13
y = 0.13 e-0.04 x
R2 = 0.20
y = 0.14 e-0.05 x
R2 = 0.13
Axis title is depending on the symbols (see the legend), and unit is %
Carbonate cements
Quartz cement
Sencondary porosity
Total clay minerals
Chlorite

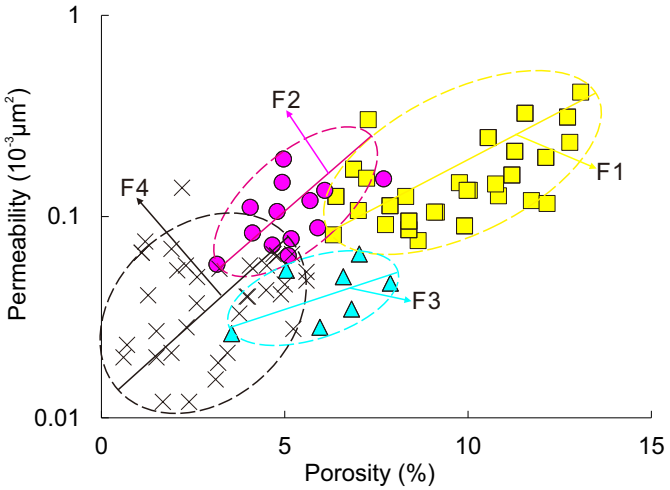
1
0.1
0.01
Permeability (10-3µm2)
0
5
10
15
Porosity (%)
F1
F2
F3
F4

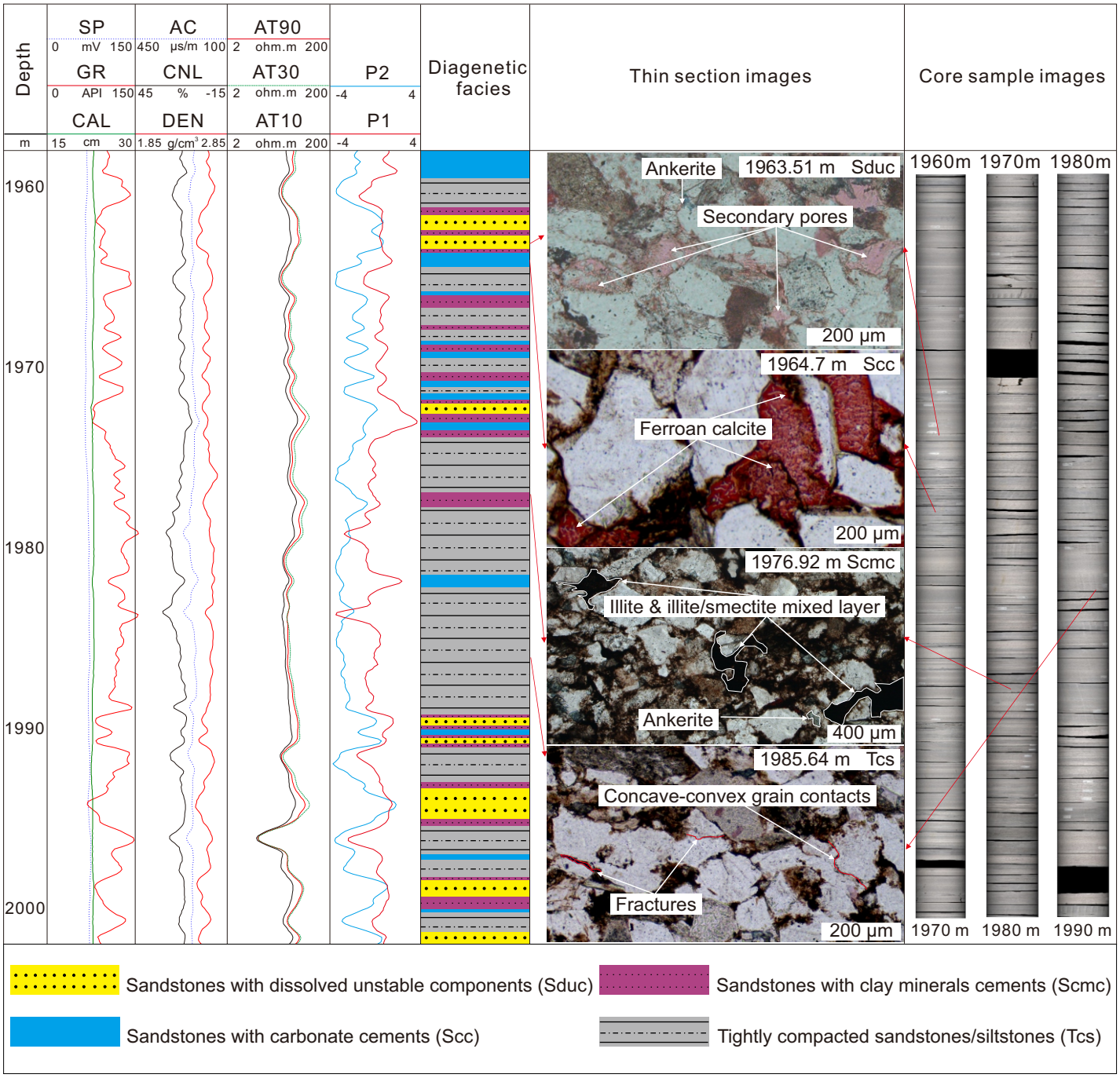
Depth
SP
0 mV 150
GR
0 API 150
CAL
m 15 cm 30
AC
450 μs/m 100
CNL
45 % -15
DEN
1.85 g/cm³ 2.85
AT90
2 ohm.m 200
AT30
2 ohm.m 200
AT10
2 ohm.m 200
P2
-4 4
P1
-4 4
Diagenetic facies
Thin section images
Core sample images
1960
1970
1980
1990
2000
Ankerite
1963.51 m Sduc
Secondary pores
200 μm
1964.7 m Scc
Ferroan calcite
200 μm
1976.92 m Scmc
Illite & illite/smectite mixed layer
Ankerite
400 μm
1985.64 m Tcs
Concave-convex grain contacts
Fractures
200 μm
1960m 1970m 1980m
1970 m 1980 m 1990 m
Sandstones with dissolved unstable components (Sduc)
Sandstones with clay minerals cements (Scmc)
Sandstones with carbonate cements (Scc)
Tightly compacted sandstones/siltstones (Tcs)

Diagenetic facies	Porosity (%)		Permeability (10^{-3}μm^2)		TS porosity (%)		Density (g/cm^3)		Grain contact types	Mean grain size (μm)	Sorting	Composition
	Range	Av.	Range	Geomean	Range	Av.	Range	Av.				
Sst with dissolved unstable components	6.3-13.1	9.7	0.076-0.432	0.15	3.8-9.5	5.9	2.39-2.56	2.47	PC & LC	209	MW-W	FL & LA
Sst with clay minerals cements	3.2-7.7	5.1	0.058-0.193	0.102	1.0-2.8	1.8	2.41-2.62	2.53	PC, LC & CCC	159	MW	FL & L
Sst with carbonate cements	3.6-7.9	6.1	0.026-0.065	0.049	0.8-2.2	1.6	2.48-2.71	2.62	PC & LC	176	MW-W	FL
Tightly compacted sst/siltst	0.6-5.6	3.1	0.012-0.139	0.04	<1.8	0.9	2.45-2.67	2.58	LC, CCC & SC	94	MW	FL & L

sst = sandstones; siltst = siltstones; Av. = average; TS = thin section; PC = point contact; LC = long contact; CCC = concave-convex contact; SC = sutured contact; MW = moderately well; W = well; FL = feldspathic litharenite; LA = lithic arkose; L = litharenite

Diagenetic facies	AC (μs/m)		CNL (%)		DEN (g/cm^3)		GR (API)		RT(Ω·m)		SP (mV)	
	Range	Av.	Range	Av.	Range	Av.	Range	Av.	Range	Av.	Range	Av.
Sst with dissolved unstable components	206-252	232	11.2-27.1	17.8	2.417-2.594	2.512	68-102	85	22-90	49	2.1-6.7	3.5
Sst with clay minerals cements	207-229	221	10.9-16.8	13.3	2.548-2.616	2.583	76-104	89	27-60	50	2.2-4.2	3.3
Sst with carbonate cements	203-228	218	10.7-16.3	12.7	2.581-2.696	2.626	83-100	87	31-73	54	2.3-4.5	3.5
Tightly compacted sst/siltst	217-258	230	12.4-47.2	19.1	2.489-2.646	2.595	95-154	113	7.5-55	33	1.2-5.5	3.1

sst = sandstones; siltst = siltstones; Av. = average

Biplots	GR vs. DEN				GR vs. CNL				GR vs. AC				GR vs. RT				P1 vs. P2				P2 vs. P3			
Diagenetic Facies	D1	D2	D3	D4	D1	D2	D3	D4	D1	D2	D3	D4	D1	D2	D3	D4	D1	D2	D3	D4	D1	D2	D3	D4
Success (%)	87	45	92	97	76	12	14	96	75	15	8	98	48	0	7	93	98	87	89	99	29	29	9	59
Overlap 1 (%)	13	55	8	3	21	78	66	3	12	47	41	2	44	77	32	2	2	13	11	1	45	16	23	38
Overlap 2 (%)	0	0	0	0	3	10	20	1	12	35	46	0	8	21	57	4	0	0	0	0	26	54	67	2
Overlap 3 (%)	0	0	0	0	0	0	0	0	1	3	5	0	0	2	4	1	0	0	0	0	0	1	1	1

D1 = sandstones with dissolved unstable components; D2 = sandstones with clay minerals cements; D3 = sandstones with carbonate cements; D4 = tightly compacted sandstones/siltstones; Success = when the technique successfully predicted the diagenetic facies; Overlap 1, 2, 3 = the technique predicted more than one diagenetic facies i.e. two, three and four diagenetic facies at a depth respectively.